Three-dimensional modeling of the plasma arc in arc welding

G. Xu,[1] J. Hu,[2,a)] and H. L. Tsai[1]
[1]*Department of Mechanical and Aerospace Engineering, Missouri University of Science and Technology (formerly University of Missouri-Rolla), 1870 Miner Circle, Rolla, Missouri 65409, USA*
[2]*Department of Mechanical Engineering, University of Bridgeport, Bridgeport, Connecticut 06604, USA*

(Received 29 April 2008; accepted 23 August 2008; published online 17 November 2008)

Most previous three-dimensional modeling on gas tungsten arc welding (GTAW) and gas metal arc welding (GMAW) focuses on the weld pool dynamics and assumes the two-dimensional axisymmetric Gaussian distributions for plasma arc pressure and heat flux. In this article, a three-dimensional plasma arc model is developed, and the distributions of velocity, pressure, temperature, current density, and magnetic field of the plasma arc are calculated by solving the conservation equations of mass, momentum, and energy, as well as part of the Maxwell's equations. This three-dimensional model can be used to study the nonaxisymmetric plasma arc caused by external perturbations such as an external magnetic field. It also provides more accurate boundary conditions when modeling the weld pool dynamics. The present work lays a foundation for true three-dimensional comprehensive modeling of GTAW and GMAW including the plasma arc, weld pool, and/or electrode. © *2008 American Institute of Physics*. [DOI: 10.1063/1.2998907]

I. INTRODUCTION

Gas tungsten arc welding (GTAW) and gas metal arc welding (GMAW) are both the arc welding processes that use a plasma arc between two opposite polarities—an electrode and a workpiece, as shown in Fig. 1 of a GMAW. A complete model for an arc welding process should include three components—the electrode, workpiece (weld pool), and plasma arc. According to a survey article,[1] models of each separate component are categorized as the first-generation arc welding models. While in the second-generation models, two or three components are integrated into a more comprehensive system. Among the three components, plasma arc is the most important one because it carries the electric current and welding energy and provides the boundary conditions for the models of other components. Two-dimensional axisymmetric plasma arc models were well formulated.[2–20] Most weld pool models (first-generation) excluded the modeling of plasma arc and used presumed Gaussian distributions of the arc pressure, heat flux, and electric current density.[1] The selection of Gaussian parameters is rather arbitrary and can be adjusted in accordance to experimental measurements. Likewise, in a first-generation electrode model on the droplet generation for GMAW the distributions of electric current density and heat flux are approximated by given formulas based on experimental results.[21–26] The separate or first-generation models are generally able to achieve reasonable numerical results if appropriate parameters are chosen, but the presumed boundary conditions are arbitrary and may not represent the real situation. Thus, more rigorous models, i.e., second-generation models, are being developed that integrate the two or three components completely.[1] These models treated the arc-weld pool and arc-electrode boundaries as coupled internal boundaries and, therefore, eliminated the assumptions required for each separate component.[27,28] Hu and Tsai[29,30] studied the metal transfer and arc plasma in the GMAW process using such a completely integrated two-dimensional model.

Most existing arc welding models are two-dimensional that are suitable to simulate the stationary axisymmetric arc and are relatively less complicated in formulation and computation. Although three-dimensional arc welding models focusing on the weld pool (with or without droplet impingement) have been developed, the two-dimensional axisymmetric Gaussian assumption was still assumed in these three-dimensional models.[31–33] They are not true three-dimensional models as, in reality, the moving arc is nonaxisymmetric. Even for the stationary arc, some external perturbations such as the external magnetic field may deflect the arc from its axisymmetry.[34] To capture any nonaxisymmetric effects, a true three-dimensional plasma arc model is a must. This article presents the mathematical formulation of a three-dimensional plasma arc model and the computational results.

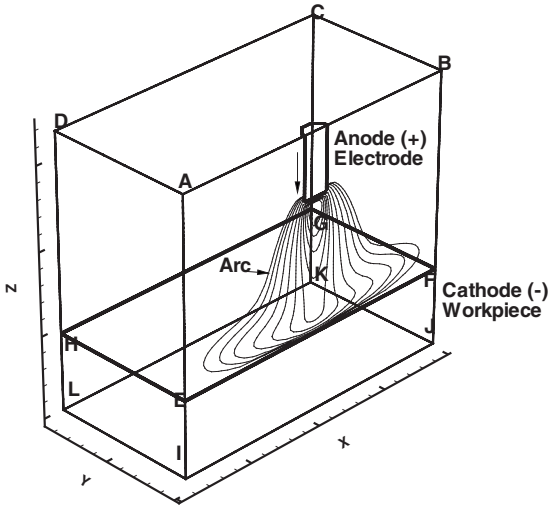

FIG. 1. A schematic representation of a GMAW system.

[a)]FAX: +1-203-576-4765. Electronic mail: jjhu@bridgeport.edu.

The ultimate goal of this work is to unify the present arc model with the weld pool and/or electrode models for a completely integrated three-dimensional model for GTAW or GMAW.

The major difficulty in three-dimensional modeling of the plasma arc is the calculation of the self-induced magnetic field, which is required to compute the electromagnetic force for momentum equations. In the axisymmetric case, the calculation of the azimuthal magnetic field B_θ is simply derived from Ampere's law[2]

$$B_\theta = \frac{\mu_0}{r}\int_0^r J_z r dr,$$

where μ_0 is the magnetic permeability of vacuum, r is the radial distance, and J_z is the axial current density that can be solved from the current continuity equation and Ohm's law. The three-dimensional magnetic field may not be azimuthal and cannot be easily calculated. One approach to calculate the nonazimuthal magnetic field is to solve the integration from Biot–Savart's law.[34] The magnetic field vector at a point A is given by

$$\vec{B}_A = \int\int\int_{\text{for all } Q} \frac{\mu_0}{4\pi}\frac{\vec{j}_Q \times \vec{r}_{QA}}{|\vec{r}_{QA}|^3} dV_Q,$$

where $\vec{j}_Q$ is the current density vector at a source volume Q and $\vec{r}_{QA}$ is the vector between a source volume Q and the point under consideration A. It can be found that for each point A a triple integration has to be computed. The time complexity for this algorithm is $n^3 \times n^3 = n^6$, where n is the number of grids in each dimension of the computation domain. The computation for this algorithm is extremely intensive or time consuming.

In this article, a Poisson equation for the magnetic field vector is derived from Ampere's law. As the Poisson equation contains the electric current density vector, this equation is coupled with the current continuity equation. By simultaneously solving all these equations in addition to the well-formulated conservation equations of mass, momentum, and energy, the three-dimensional plasma arc can be simulated. The time complexity required to calculate the magnetic field vector has been reduced to the order of n^3.

II. MATHEMATICAL MODEL

A. Governing equations

Figure 1 is the schematic sketch of a GMAW process, which is used as the study case in this article. In the arc welding process, a constant current is applied to the electrode and a plasma arc is struck between the electrode and the workpiece. The computational domain includes an anode region, an arc region, and a cathode region. For the GMAW case, the electrode is the anode, and the workpiece is the cathode. The domain is symmetric in y direction, i.e., the plane BAIJ is the symmetric plane. The mathematical formulation of the plasma flow is the three-dimensional extension from a two-dimensional version in Ref. 2. Some assumptions made in the model are: (1) the arc is in local thermal equilibrium (LTE), (2) the gas flow is laminar, (3) the plasma is optically thin and the radiation is modeled using an optical thin radiation loss per unit volume, (4) the electrode is cylindrical and the tip of the electrode and the workpiece surface are flat, and (5) the consumable electrode is in quasi-steady state and the influence of metal droplets is neglected. The velocity, pressure, and temperature are computed for the arc region because the plasma flow is confined in this region only, while the electric potential, electric current density, and magnetic field are computed for the whole domain. The governing equations for the plasma arc are given below as follows:

(1) Mass continuity

$$\frac{\partial \rho}{\partial t} + \nabla \cdot (\rho \vec{V}) = 0. \tag{1}$$

(2) Momentum

$$\frac{\partial(\rho u)}{\partial t} + \nabla \cdot (\rho \vec{V} u) = -\frac{\partial p}{\partial x} + \frac{\partial}{\partial x}\left[\mu\left(2\frac{\partial u}{\partial x} - \frac{2}{3}\nabla \cdot \vec{V}\right)\right] + \frac{\partial}{\partial y}\left[\mu\left(\frac{\partial u}{\partial y} + \frac{\partial v}{\partial x}\right)\right] + \frac{\partial}{\partial z}\left[\mu\left(\frac{\partial u}{\partial z} + \frac{\partial w}{\partial x}\right)\right] + j_y B_z - j_z B_y, \tag{2}$$

$$\frac{\partial(\rho v)}{\partial t} + \nabla \cdot (\rho \vec{V} v) = -\frac{\partial p}{\partial y} + \frac{\partial}{\partial y}\left[\mu\left(2\frac{\partial v}{\partial y} - \frac{2}{3}\nabla \cdot \vec{V}\right)\right] + \frac{\partial}{\partial z}\left[\mu\left(\frac{\partial v}{\partial z} + \frac{\partial w}{\partial y}\right)\right] + \frac{\partial}{\partial x}\left[\mu\left(\frac{\partial v}{\partial x} + \frac{\partial u}{\partial y}\right)\right] + j_z B_x - j_x B_z, \tag{3}$$

$$\frac{\partial(\rho w)}{\partial t} + \nabla \cdot (\rho \vec{V} w) = -\frac{\partial p}{\partial z} + \frac{\partial}{\partial z}\left[\mu\left(2\frac{\partial w}{\partial z} - \frac{2}{3}\nabla \cdot \vec{V}\right)\right] + \frac{\partial}{\partial x}\left[\mu\left(\frac{\partial w}{\partial x} + \frac{\partial u}{\partial z}\right)\right] + \frac{\partial}{\partial y}\left[\mu\left(\frac{\partial w}{\partial y} + \frac{\partial v}{\partial z}\right)\right] + j_x B_y - j_y B_x. \tag{4}$$

(3) Energy

$$\frac{\partial(\rho h)}{\partial t} + \nabla \cdot (\rho \vec{V} h) = \nabla \cdot \left(\frac{k}{c_p}\nabla h\right) + \frac{j_x^2 + j_y^2 + j_z^2}{\sigma_e} - S_R + \frac{5k_b}{2e}\left(\frac{j_x}{c_p}\frac{\partial h}{\partial x} + \frac{j_y}{c_p}\frac{\partial h}{\partial y} + \frac{j_z}{c_p}\frac{\partial h}{\partial z}\right). \tag{5}$$

In Eqs. (1)–(5), t is the time, u, v, and w are, respectively, the velocity components in the x, y, and z directions, $\vec{V}$ is the velocity vector, p is the pressure, h is the enthalpy, ρ is the density, μ is the viscosity, k is the thermal conductivity, c_p is the specific heat at constant pressure, σ_e is the

TABLE I. Boundary conditions for momentum and energy equations.

	BCKJ	ADLI	CDLK	BAIJ	ABCD	IJKL
u	$\partial(\rho u)/\partial x=0$	$\partial(\rho u)/\partial x=0$	$\partial u/\partial y=0$	$\partial u/\partial y=0$	0	... [a]
v	$\partial v/\partial x=0$	$\partial v/\partial x=0$	$\partial(\rho v)/\partial y=0$	0	0	... [a]
w	$\partial w/\partial x=0$	$\partial w/\partial x=0$	$\partial w/\partial y=0$	$\partial w/\partial y=0$	$\partial(\rho w)/\partial z=0$	... [a]
	$T=300$ K (inflow)	$T=300$ K (inflow)	$T=300$ K (inflow)	$\partial T/\partial y=0$	$T=300$ K (inflow)	
h				$\partial T/\partial y=0$		... [a]
	$\partial T/\partial x=0$ (outflow)	$\partial T/\partial x=0$ (outflow)	$\partial T/\partial y=0$ (outflow)		$\partial T/\partial z=0$ (outflow)	

[a]Momentum and energy equations not solved in the solid domain.

electric conductivity, S_R is the radiation loss term, k_b is the Boltzmann constant, e is the elementary charge, j_x, j_y, and j_z are the current density components in the x, y, and z directions, respectively, and B_x, B_y, and B_z are the magnetic field components in the x, y, and z directions, respectively. The last two terms in the momentum Eqs. (2)–(4) represent the respective components of the electromagnetic force vector $\vec{j}\times\vec{B}$. The last three terms in Eq. (5) are, respectively, the Ohmic heating, radiation loss, and electron enthalpy flow (Thompson effect).

The current density components j_x, j_y, and j_z required in Eqs. (2)–(5) are obtained by solving for the electric potential ϕ from the following current continuity equation:

$$\nabla\cdot(\sigma_e\nabla\phi)=\frac{\partial}{\partial x}\left(\sigma_e\frac{\partial\phi}{\partial x}\right)+\frac{\partial}{\partial y}\left(\sigma_e\frac{\partial\phi}{\partial y}\right)+\frac{\partial}{\partial z}\left(\sigma_e\frac{\partial\phi}{\partial z}\right)=0 \tag{6}$$

and using Ohm's law

$$j_x=-\sigma_e\frac{\partial\phi}{\partial x},\quad j_y=-\sigma_e\frac{\partial\phi}{\partial y},\quad j_z=-\sigma_e\frac{\partial\phi}{\partial z}. \tag{7}$$

The magnetic field components B_x, B_y, and B_z are required to calculate the electromagnetic forces for momentum Eqs. (2)–(4). The equations needed to calculate the magnetic field can be derived from Ampere's law $\nabla\times\vec{B}=\mu_0\vec{j}$.[10] By taking the cross product on both sides and applying the following vector identity

$$\nabla\times(\nabla\times\vec{B})=-\nabla^2\vec{B}+\nabla(\nabla\cdot\vec{B})=-\nabla^2\vec{B}, \tag{8}$$

where $\nabla\cdot\vec{B}=0$ is basically the Gauss's law for magnetism, which means the absence of magnetic monopoles. The Ampere's law can be rewritten in the following conservation form[35]

$$\nabla^2\vec{B}=-\mu_0(\nabla\times\vec{j}). \tag{9}$$

Equation (9) is the Poisson vector equation and has the following three components

$$\frac{\partial^2B_x}{\partial x^2}+\frac{\partial^2B_x}{\partial y^2}+\frac{\partial^2B_x}{\partial z^2}=-\mu_0\left(\frac{\partial j_z}{\partial y}-\frac{\partial j_y}{\partial z}\right), \tag{10}$$

$$\frac{\partial^2B_y}{\partial x^2}+\frac{\partial^2B_y}{\partial y^2}+\frac{\partial^2B_y}{\partial z^2}=-\mu_0\left(\frac{\partial j_x}{\partial z}-\frac{\partial j_z}{\partial x}\right), \tag{11}$$

$$\frac{\partial^2B_z}{\partial x^2}+\frac{\partial^2B_z}{\partial y^2}+\frac{\partial^2B_z}{\partial z^2}=-\mu_0\left(\frac{\partial j_y}{\partial x}-\frac{\partial j_x}{\partial y}\right). \tag{12}$$

The governing equations are now complete. This system of equations has 12 unknowns, u, v, w, p, h, ϕ, j_x, j_y, j_z, B_x, B_y, and B_z, and is closed by 12 differential equations, Eqs. (1)–(7) and Eqs. (10)–(12). Note Eq. (7) is actually three equations. The supplemental boundary conditions are the next considerations in order to solve these differential equations. Compared to calculating the magnetic field from the integral form of Biot–Savart law, the solution of Eqs. (10)–(12) from three algebraic equations after discretization greatly reduces the time complexity from n^6 to n^3.

B. Momentum and energy boundary conditions for the arc

1. Metal regions (workpiece and electrode)

The present study excludes the computation of the molten metal flow and energy transfer in the workpiece and electrode. Therefore, the momentum and energy equations are not solved in the metal regions. The momentum and temperature boundary conditions need to be set at the boundaries between the arc and the metal regions.

The no-slip boundary condition is simply imposed for the momentum boundary conditions. The temperature boundary condition at the anode (electrode) T_a is assumed to be the melting temperature of pure iron, 1810 K, and the

TABLE II. Boundary conditions for electric potential and magnetic field equations.

	BCKJ	ADLI	CDLK	BAIJ	ABCD	IJKL
ϕ	$\partial\phi/\partial x=0$	$\partial\phi/\partial x=0$	$\partial\phi/\partial y=0$	$\partial\phi/\partial y=0$	$-\sigma_e\partial\phi/\partial z=I/\pi R_a^2$, $r<R_a$ [a] $\partial\phi/\partial z=0$, $r>R_a$ [a]	0
B_x	$\partial B_x/\partial x=0$	$\partial B_x/\partial x=0$	$\partial B_x/\partial y=0$	0	$y/r(\mu_0 I/2\pi r)$, $r>R_a$ [a] $y/r(r\mu_0 I/2\pi R_a^2)$, $r<R_a$ [a]	$\partial B_x/\partial z=0$
B_y	$\partial B_y/\partial x=0$	$\partial B_y/\partial x=0$	$\partial B_y/\partial y=0$	$\partial B_y/\partial y=0$	$-x/r(\mu_0 I/2\pi r)$, $r>R_a$ [a] $-x/r(r\mu_0 I/2\pi R_a^2)$, $r<R_a$ [a]	$\partial B_y/\partial z=0$
B_z	$\partial B_z/\partial x=0$	$\partial B_z/\partial x=0$	$\partial B_z/\partial y=0$	$\partial B_z/\partial y=0$	0	$\partial B_z/\partial z=0$

[a]R_a is the radius of the electrode and $r=\sqrt{x^2+y^2}$.

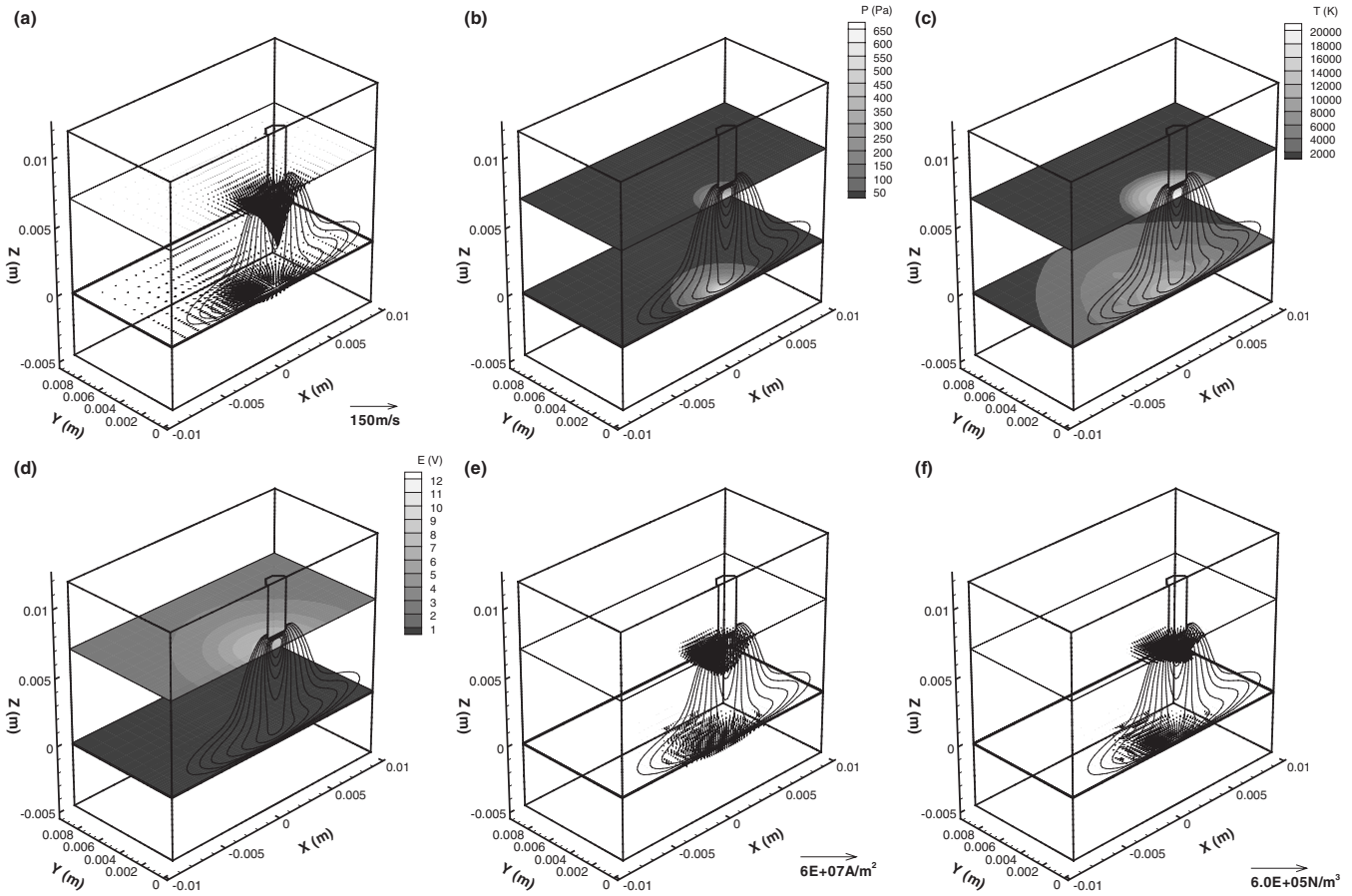

FIG. 2. Three-dimensional vectors or contour distributions at $z=0.1$ mm (just above the workpiece) and $z=7$ mm (1 mm below the electrode tip): (a) velocity, (b) pressure, (c) temperature, (d) electric potential, (e) electric current density, and (f) electromagnetic force.

temperature at cathodes (workpiece) T_c is assumed to be 1000 K. Apparently, the temperature in the electrode and the workpiece may differ, but the difference has little effect on the arc column, which has been demonstrated through sensitivity studies.[2]

2. Arc region

The complete listing of the momentum and energy boundary conditions for the arc region is given in Table I. The top plane ABCD is the inflow anode region. The velocity components in x and y directions are assumed to be zero and the gradient of mass flow $\partial(\rho w)/\partial z$ in z direction is assumed to be zero. The density ρ is included in the partial derivative expression to ensure the mass conservation. The inlet gas temperature is assumed to be 300 K. Sensitivity analyses have shown the inlet temperature has an insignificant effect on the arc column.[2]

For the side planes, it is not clear where the inflow and outflow will occur. The gradient of mass flow $\partial(\rho u)/\partial x$ is assumed to be zero for the planes ADHE and BCGF. $\partial(\rho v)/\partial y$ is assumed to be zero for the plane CDHG. The temperature boundary condition representing the inflow is taken as 300 K. This value is arbitrary and the sensitivity studies have shown that the arc column is not affected significantly by this temperature value.[2] This is because the variation in specific heat outside the arc column is very small and does not cause a large change to the energy equation.[2] For the outflow, the gradients of temperature, $\partial T/\partial x$ and $\partial T/\partial y$, are assumed to be zero.

The boundary conditions at the symmetric plane BAEF is straightforward. The velocity component in y direction is zero. The gradients of velocity $\partial u/\partial y$ and $\partial w/\partial y$ and the gradient of temperature $\partial T/\partial y$ are zero.

C. Electric potential and magnetic field boundary conditions

The boundary conditions for the electric potential and the magnetic field need to be imposed for the whole domain. The complete listing of electric potential and magnetic field boundary conditions is given in Table II. The bottom plane of the workpiece IJKL is taken to be isopotential ($\phi=0$). The welding current is assumed to be uniformly distributed when it flows into the electrode. The gradient of electric potential for the electrode boundary becomes

$$-\sigma_e \frac{\partial \phi}{\partial z} = \frac{I}{\pi R_a^2}, \quad r < R_a, \tag{13}$$

where $r=\sqrt{x^2+y^2}$ is the distance from the electrode axis, R_a is the radius of the electrode, and I is the welding current. The gradient of electric potential for the top boundary plane ($r>R_a$), the symmetric plane, and all side boundary planes are assumed to be zero.

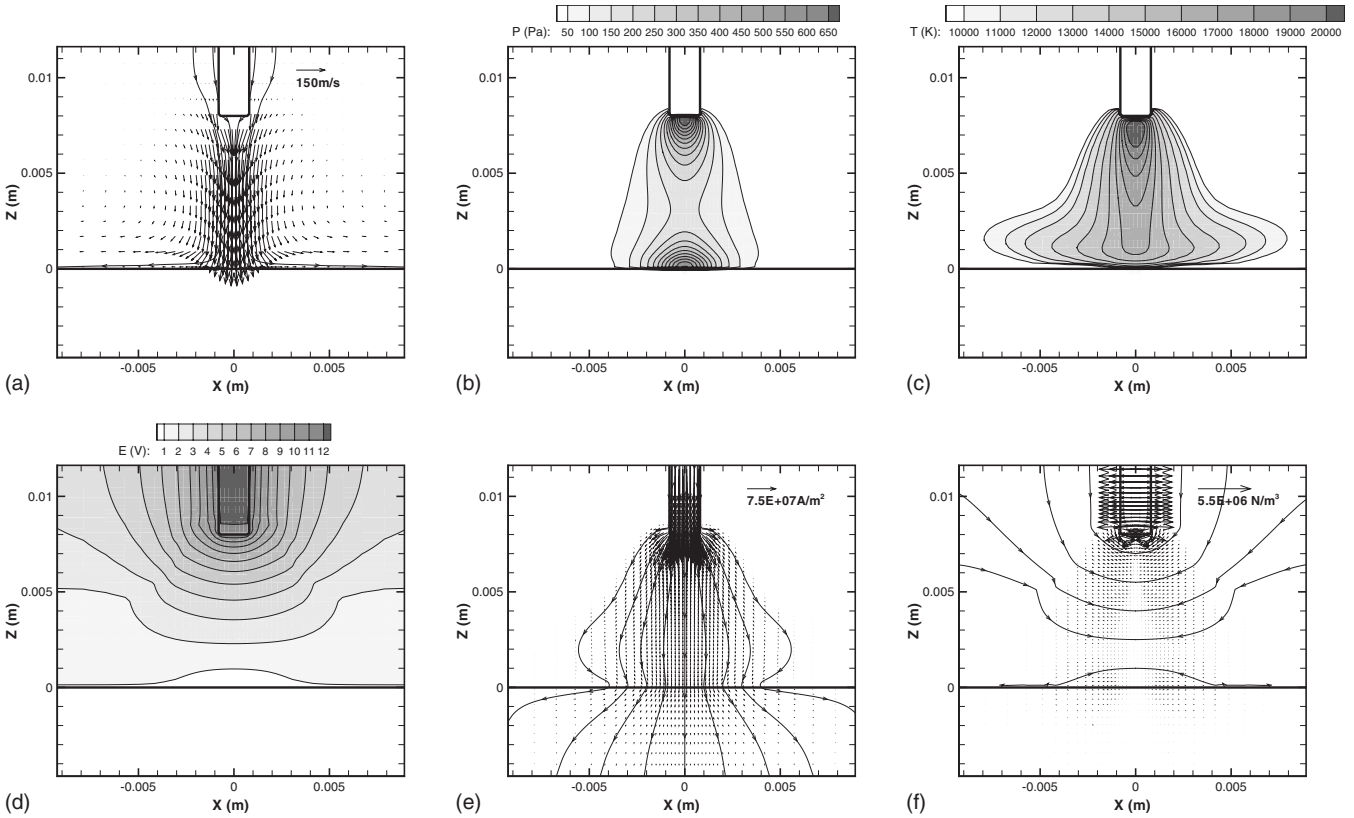

FIG. 3. Two-dimensional vectors with streamlines or contour distributions at the symmetric plane ($y=0$): (a) velocity, (b) pressure, (c) temperature, (d) electric potential, (e) electric current density, and (f) electromagnetic force.

The magnetic field at the top plane ABCD is assumed to be azimuthal. From Ampere's law, the azimuthal magnetic field B_θ is given as

$$B_\theta = \frac{r\mu_0 I}{2\pi R_a^2}, \quad r < R_a, \tag{14}$$

$$B_\theta = \frac{\mu_0 I}{2\pi r}, \quad r > R_a. \tag{15}$$

The projected x and y components are

$$B_x = \frac{y}{r}B_\theta, \quad B_y = -\frac{x}{r}B_\theta, \tag{16}$$

where the signs of B_x and B_y account for the direction of welding current (anode electrode in the GMAW case). The z component is zero for the azimuthal assumption.

For all the side planes and the bottom plane of the workpiece, the gradient of magnetic field is simply assumed to be zero. For the symmetric plane BAIJ, B_x is zero and the gradients of magnetic field $\partial B_y/\partial y$ and $\partial B_z/\partial y$ are zero.

D. Energy source terms at the metal regions

1. Anode region (electrode)

At the arc-anode interface, there exists an anode sheath region.[6] In this region, the mixture of plasma and metal vapor departs from LTE and, thus the present model is not valid. Some plasma arc models considered the formulation of the anode sheath region,[10] but many just simply neglected it and reasonable results were still obtained.[2–5] This article adopts the latter simplification. The heat losses in the arc-anode interface are only those due to the Thompson effect (transport of electron enthalpy) and the conduction.[2] Hence, the energy source term at the anode boundary can be represented by

$$S_a = \frac{5}{2}\frac{k_b}{e}[j_a(T_{\text{arc}} - T_a)] + k\frac{T_{\text{arc}} - T_a}{\delta}, \tag{17}$$

where the first term represents the Thompson effect and it may have three components each in the x, y, and z directions. The second term represents the heat conduction; j_a is the current density at the anode (electrode), T_a is the temperature of the anode, and T_{arc} is the temperature of the gas at a distance δ from the anode. This distance δ (=0.1 mm) is the maximum experimentally observed thickness of the anode fall region. This approach is an approximation since the size of the anode fall region is unknown. However, sensitivity analyses showed the arc is less dependent on δ.[2]

2. Cathode region (workpiece)

Similar to the anode region, there exists a cathode sheath region at the arc-cathode interface where non-LTE condition occurs. However, the physics of the cathode sheath and the energy balance at the nonthermionic cathode (in the GMAW case) are not well understood.[36] Therefore, the energy source term at the cathode boundary is treated as that used in GTAW. This is again an approximation, but the sensitivity

calculation showed it will not affect the arc column much.[2] The energy source term at the cathode boundary is expressed as

$$S_c = |j_c| V_c, \tag{18}$$

$$V_c = \frac{5}{2} \frac{k_b (T_{\text{arc}} - T_c)}{e}, \tag{19}$$

where V_c is the cathode fall voltage, T_c is the temperature of the cathode (workpiece), and T_{arc} is the temperature of the gas at a distance 0.1 mm from the cathode. This distance is the maximum experimentally observed thickness of the cathode fall region.[2]

III. THERMOPHYSICAL PROPERTIES OF GAS

Thermophysical properties of the shielding gas (argon in the present study) are highly temperature dependent. Properties such as molecular viscosity, thermal conductivity, and electrical conductivity for argon (Ar) are taken from tabulated data of Devoto.[36] Linear interpolation is employed for properties at temperatures other than tabulated values. The gas density is calculated by the equation of state.[36] It is the only thermophysical property that is not from tabulated data. This is because the equations for gas density are relatively simple and accurate. The equation of state for plasma gas is

$$p = (1 + \alpha) n k T, \tag{20}$$

where α is the degree of ionization and n is the initial concentration of neutral atoms. The degree of ionization is defined as the ratio between the ionized atoms to the initial neutral atoms. If the mass of the argon atom is m_{Ar}, the gas density is given by

$$\rho = m_{\text{Ar}} n = \frac{m_{\text{Ar}} p}{k_b T (1 + \alpha)}. \tag{21}$$

The degree of ionization may be computed from the Saha equation for single ionization of argon (single ionization is assumed in the present study).[36]

$$\frac{\alpha^2}{1 - \alpha^2} p/p_0 = 1.264 \times 10^{-6} T^{5/2} \times (2 + e^{-2062/T}) \times e^{-183000/T}, \tag{22}$$

where p_0 is the pressure of standard atmosphere, 101 325 Pa. In the present study, the plasma pressure is set as the atmospheric pressure (not the high-pressure arc). p/p_0 can be taken to one because the arc pressure is relatively small in comparison to the atmospheric pressure. This will be justified by the computational results on the arc pressure to be discussed next.

IV. NUMERICAL CONSIDERATIONS

In the present study, a steady solution of the governing equations is sought. The SIMPLE algorithm[37] is applied to solve the conservation equations of mass and momentum to obtain the velocity and pressure fields. Since the nonlinear governing equations are highly temperature dependent, the relaxation factor as small as 0.3 is used to ensure the convergence.

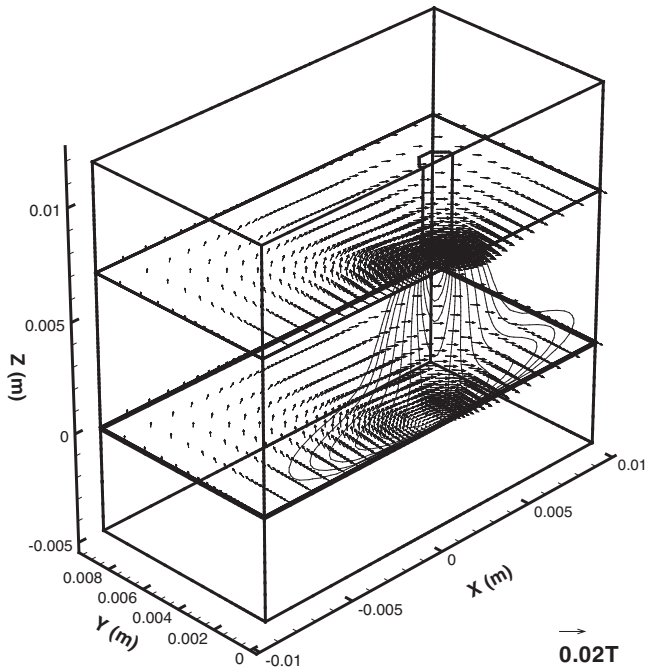

FIG. 4. Magnetic field vectors at $z=0.1$ mm (just above the workpiece) and $z=7$ mm (1 mm below the electrode tip).

The system of differential equations is solved for the steady state solution through the following time-marching scheme:

(1) The current continuity equation is solved first, based on the updated properties (the initial settings can be arbitrary).
(2) Current density and the source term for Poisson magnetic field equations are then calculated.
(3) The magnetic field equations are solved and the electromagnetic forces are then calculated for the momentum equations.
(4) The conservation equations of mass and momentum are solved to obtain the pressure and velocity fields.
(5) The energy equation is solved to get the new temperature distribution.
(6) The temperature-dependent properties are updated and the program marches to the next time step and goes back to step 1. The time marching continues until the converged solution is reached. At that time, the steady state solution is achieved.

A typical computation uses a $40 \times 20 \times 70$ nonuniform mesh. The mesh size near the anode axis is set as 0.2 mm. The computation time is about 4 h on the latest DELL PCs with a Linux operating system.

V. RESULTS AND DISCUSSION

The electrode is assumed to be mild steels with a 1.6 mm diameter. The workpiece is a mild steel chunk with a 5 mm thickness. The properties of mild steels are from Ref. 27. The shielding gas is argon (Ar). The initial arc length is set as 8 mm. The welding current chosen in this study is 220 A. Two

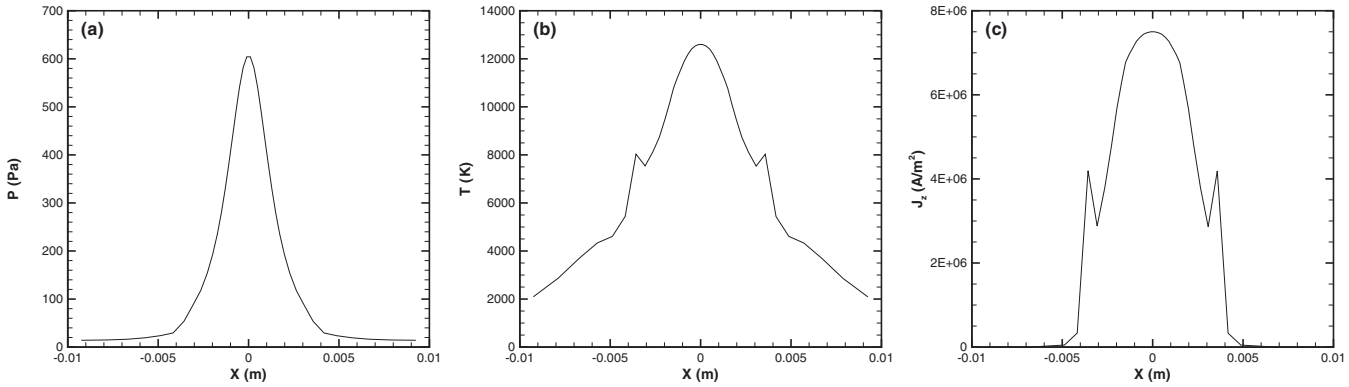

FIG. 5. Distributions at the workpiece surface: (a) pressure, (b) temperature, and (c) current density J_z.

cases are studied in this article. The first case is for a stationary axisymmetric arc. Although this case can be done by a two-dimensional axisymmetric model, it is studied first to assure the correctness of the present three-dimensional model. The computation domain for the first case is $20 \times 10 \times 17$ mm^3 and $z=0$ is set at the workpiece surface. The second case is for a stationary deflected arc. In this case the arc is nonaxisymmetric and cannot be modeled by a two-dimensional model. The computation domain in x direction for the second case is doubled to 40 mm to catch the arc deflection.

A. Axisymmetric plasma arc

Figures 2(a)–2(f) show the three-dimensional plots of the vectors of velocity, electric current density, and magnetic field and the distributions of temperature, pressure, and electric potential. They are drawn for two planes sliced at $z=0.1$ mm, which is just above the workpiece surface, and $z=7$ mm, which is 1 mm below the flat electrode tip. Figures 3(a)–3(f) show the corresponding two-dimensional plots for Figs. 2(a)–2(f) at the symmetric plane ($y=0$). The calculated highest flow velocity is in the order of 10^2 m/s. This is consistent with the two-dimensional simulation results.[2–20,27] The flow velocity in the arc can be high because the centripetal electromagnetic force drives the gas toward the high temperature arc column [Fig. 3(a)]. High velocities in this zone are required by mass continuity ($\nabla \cdot (\rho \vec{V}) = 0$). High pressure is found at the velocity stagnation (zero velocity) zones, as expected, which are under the electrode tip and above the workpiece surface [Fig. 3(b)]. The maximum pressure is below 1000 Pa and not comparable to the standard atmospheric pressure. This validates the simplification in the property calculation of gas density, as discussed previously, where the atmospheric pressure is used. The arc pressure is a remarkable attaching force during the droplet generation in the GMAW process. However, this effect has been neglected in most static force balance models.[38] The interesting thing is once a droplet detaches from the electrode, the arc pressure will accelerate the droplet transfer to the workpiece. The detailed simulation results are presented in Ref. 29. The famous "bell-shape" plasma arc is observed from Fig. 3(c). This shape can be seen in many published photographs of the plasma arc. The highest temperature of the arc column is over 20 000 K. Temperatures at this range were obtained from many arc models and also from experiments.[1–10,27] The high temperature arc under the electrode tip provides energy to melt the electrode and generates droplets in the GMAW process.

The electric potential (voltage) drop is 12.4 V from the electrode to the workpiece. This value agrees with the two-dimensional simulation result.[27] The gradients of electric potential are greater in the plasma side around the electrode tip. This is determined by the current continuity ($\nabla \cdot \vec{j} = 0$ and $\vec{j} = \sigma_e \nabla \phi$) since the electric conductivity σ_e of the plasma is much smaller than that of metal (order of magnitude). The electric current density leaks from the electrode tip and converges to a circular shape at the surface of the workpiece, as shown in Figs. 2(e) and 3(e). The electric current then diminishes quickly below the surface in the workpiece. The current convergence produces a local current peak at the surface of the workpiece, which in turn produces a temperature peak by Ohmic heating. The vectors and streamlines of electromagnetic force are shown in Figs. 2(f) and 3(f). The streamlines coincide with the contours of electric potential [Fig. 3(d)], since they are both orthogonal to the electric current. Electromagnetic force is the dominant driving force in the arc plasma flow. This force drives the gas toward the high tem-

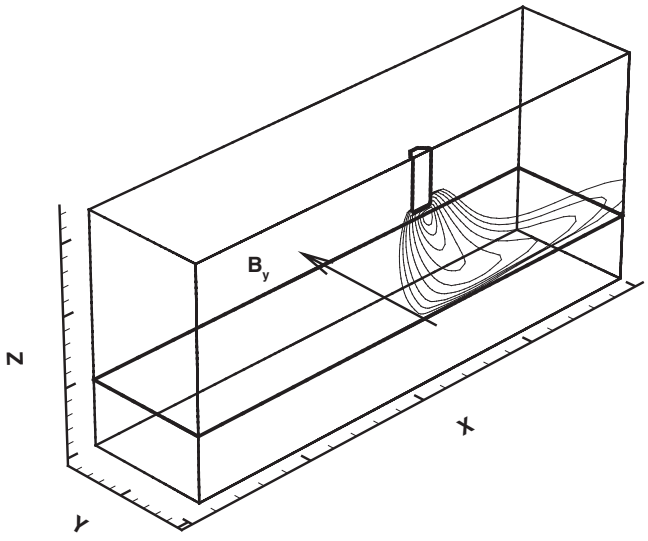

FIG. 6. A schematic representation of arc deflection.

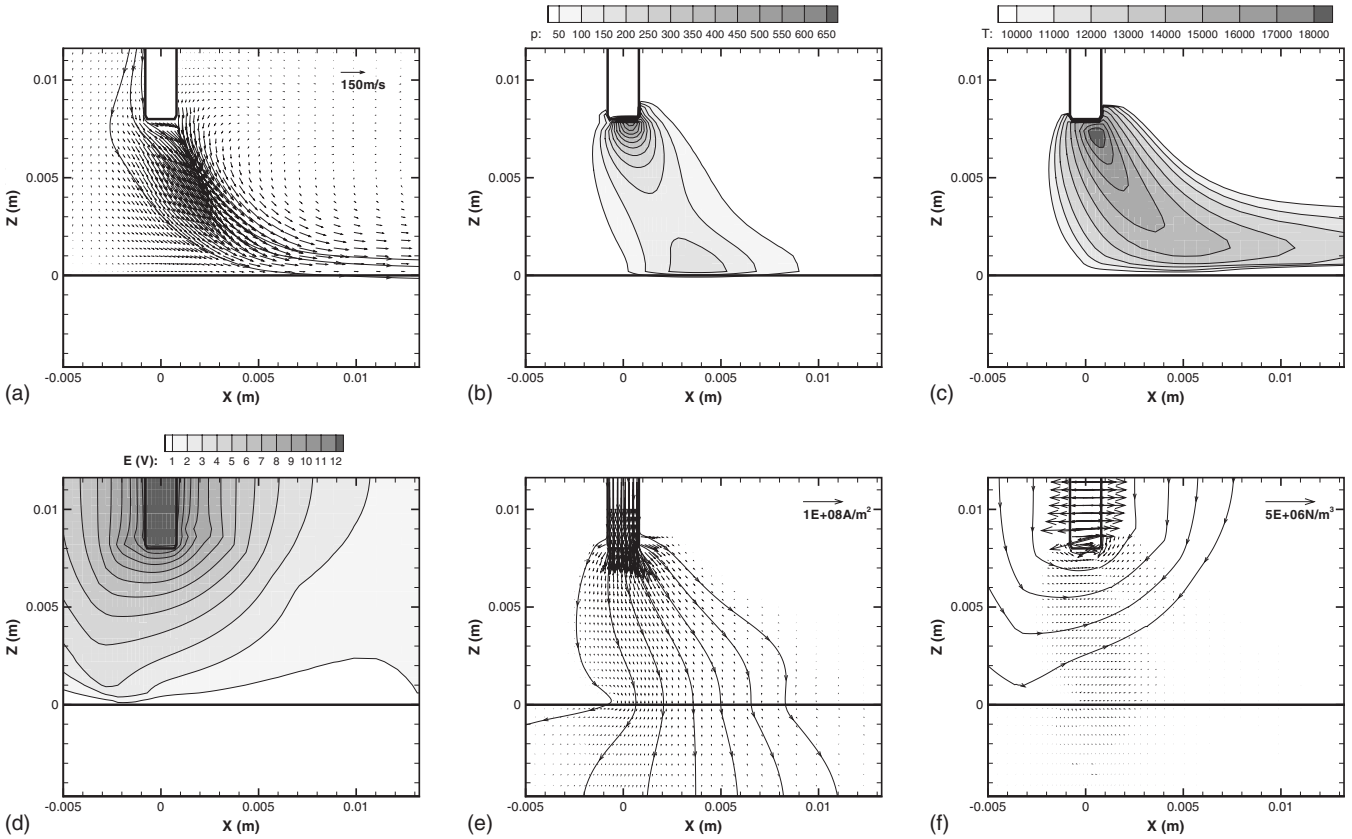

FIG. 7. Two-dimensional vectors with streamlines or contour distributions of the deflected arc at the symmetric plane ($y=0$): (a) velocity, (b) pressure, (c) temperature, (d) electric potential, (e) electric current density, and (f) electromagnetic force.

perature arc column and accelerates downward. The electromagnetic force at the electrode tip tends to taper the tip. It is the major detaching force for droplets in the GMAW process and is balanced by the surface tension force and arc pressure force before the detachment. Detailed discussions and analyses on this static force balance were given in Ref. 38. Figure 4 shows the magnetic field vectors. The azimuthal magnetic field is observed as expected for this axisymmetric study case.

The distributions of pressure, temperature, and current density J_z at the workpiece surface ($z=0.1$ mm, the nearest grid to the surface) are illustrated in Fig. 5. They are used to examine the soundness of Gaussian assumptions for these distributions. As discussed before, this assumption is employed in many weld pool models. As seen in Fig. 5(a), it is reasonable for the assumption of Gaussian pressure distribution if correct mean and variance values are selected. However, when considering the influence of metal droplets in the GMAW process, this assumption is not suitable again. Hu and Tsai[27] revealed the evolvement of the axisymmetric pressure distribution during the droplet transfer sequences. The Gaussian assumption for the temperature distribution is acceptable [Fig. 5(b)], but the variance is not the same as that of the pressure. There is an irregular peak at the periphery of the temperature dome. As discussed before, this peak resulted from the electric current peak [Fig. 5(c)] and Ohmic heating. The irregularity is caused by grid coarseness. For the distribution of the electric current density J_z, the Gaussian assumption may not be good because the current is almost confined within a circle and vanishes abruptly beyond this circle. In fact, some researchers just assumed an unreal uniform current distribution within a presumed circular region in their models.[2]

B. Deflected plasma arc

A schematic representation of the arc deflection is shown in Fig. 6, where an external magnetic field exists. According to Ref. 34, the external magnetic field can be caused by residual magnetism in ferromagnetic materials or external electric currents that are uncontrollable. However, in some cases an external magnetic field may be applied on purpose to control the plasma deflection for a better welding quality.[39] In the present study, a uniform 35 Gauss (0.0035 Tesla) external magnetic is applied in the positive y direction and no other parameters are altered except the computational domain.

Figures 7(a)–7(f) show the same two-dimensional plots for the deflected arc as those for the axisymmetric arc. The plasma arc deflects from the axis to the positive x direction and the arc length is therefore elongated. This is caused by the deflection of plasma flow, which is in turn driven by the electromagnetic force from both the self-induced and the externally applied magnetic field. The maximum flow velocity decreases to 203 m/s in comparison with 264 m/s for the axisymmetric case, and the maximum arc temperature drops to 18 840 from 21 550 K. The high pressure region on the workpiece drifts with the deflected arc and the maximum

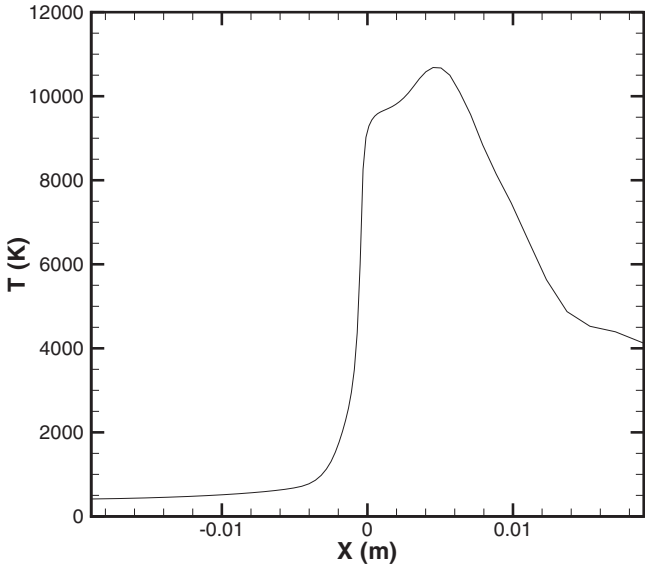

FIG. 8. Temperature distribution at the workpiece surface and along the symmetric plane ($y=0$).

pressure is 132 Pa, as compared to 604 Pa for the axisymmetric arc. The electric potential (voltage) increases to 12.7 V, a 0.3 V augment from the axisymmetric case. All these differences are the effects of the elongated plasma arc. The electric current density also drifts with the deflected arc and the electromagnetic force at the electrode tip is no longer axisymmetric. In the GMAW process, the unbalanced electromagnetic force may taper droplets to a deflected globular shape,[40] which may be caused by external magnetic perturbations.

Figure 8 shows the temperature distribution at the workpiece surface ($z=0.1$ mm) and along the symmetric plane ($y=0$). If the arc deflection length is defined as the distance between the electrode axis ($x=0$) and the highest temperature point, it can be found to be about 4.5 mm for this study case.

VI. CONCLUSIONS

A three-dimensional plasma arc model is mathematically formulated by 12 differential equations for arc welding processes such as GTAW and GMAW. It introduces a new formulation to solve for a three-dimensional magnetic field. Two cases are studied using the present model. The first case is for an axisymmetric arc, which is for validation purpose. The results from this three-dimensional model agree well with those from two-dimensional models. The second case is for a deflected arc. It is nonaxisymmetric and can only be handled by a three-dimensional model. The computational results show the deflection and other changes in the plasma arc under the effect of an external magnetic field. The future work is to unify the present three-dimensional plasma arc model with the weld pool and/or electrode droplet models to accomplish a completely integrated three-dimensional model for the GTAW and GMAW processes.

[1] P. G. Jönsson, J. Szekely, R. T. C. Choo, and T. P. Quinn, Modell. Simul. Mater. Sci. Eng. **2**, 995 (1994).
[2] P. G. Jonsson, T. W. Eagar, and J. Szekely, Metall. Mater. Trans. B **26**, 383 (1995).
[3] P. Zhu, J. J. Lowke, and R. Morrow, J. Phys. D **25**, 1221 (1992).
[4] P. Zhu, J. J. Jowke, R. Morrow, and J. Haidar, J. Phys. D **28**, 1369 (1995).
[5] J. J. Lowke, R. Morrow, and J. Haidar, J. Phys. D **30**, 2033 (1997).
[6] J. J. Lowke, P. Kovitya, and H. P. Schmidt, J. Phys. D **25**, 1600 (1992).
[7] R. T. C. Choo, J. Szekely, and R. C. Westhoff, Weld. J. **69**, 346s (1990).
[8] H. G. Fan, S.-J. Na, and Y. W. Shi, J. Phys. D **30**, 94 (1997).
[9] J. Haidar, J. Phys. D **30**, 2737 (1997).
[10] J. Haidar, J. Appl. Phys. **84**, 3518 (1998).
[11] R. J. Ducharme, P. D. Kapadia, J. Dowden, I. M. Richardson, and M. F. Thornton, J. Phys. D **29**, 2650 (1996).
[12] L. Sansonnens, J. Haidar, and J. J. Lowke, J. Phys. D **33**, 148 (2000).
[13] M. Tanaka, H. Terasaki, M. Ushio, and J. J. Lowke, Metall. Mater. Trans. A **33A**, 2002 (2002).
[14] J. Menart, J. Heberlein, and E. Pfender, J. Phys. D **32**, 55 (1999).
[15] J. Menart, S. Malik, and L. Lin, J. Phys. D **33**, 257 (2000).
[16] H. P. Schmidt and G. Speckhofer, IEEE Trans. Plasma Sci. **24**, 1229 (1996).
[17] P. G. Jonsson, R. C. Westhoff, and J. Szekely, J. Appl. Phys. **74**, 5997 (1993).
[18] P. Zhu, M. Rados, and S. W. Simpson, Plasma Sources Sci. Technol. **4**, 495 (1995).
[19] J. Haidar and J. J. Lowke, J. Phys. D **29**, 2951 (1996).
[20] J. Haidar, J. Phys. D **31**, 1233 (1998).
[21] S. K. Choi, C. D. Yoo, and Y.-S. Kim, J. Phys. D **31**, 207 (1998).
[22] S. K. Choi, C. D. Yoo, and Y.-S. Kim, Weld. J. **77**, 38s (1998).
[23] S. K. Choi, C. D. Yoo, and Y.-S. Kim, Weld. J. **77**, 45s (1998).
[24] H. G. Fan and R. Kovacevic, Metall. Mater. Trans. B **30**, 791 (1999).
[25] G. Wang, P. G. Huang, and Y. M. Zhang, Metall. Mater. Trans. B **34**, 345 (2003).
[26] F. Wang, W. K. Hou, S. J. Hu, E. Kannatey-Asibu, W. W. Schultz, and P. C. Wang, J. Phys. D **36**, 1143 (2003).
[27] J. Hu and H. L. Tsai, Int. J. Heat Mass Transfer **50**, 833 (2007).
[28] H. G. Fan and R. Kovacevic, J. Phys. D **37**, 2531 (2004).
[29] J. Hu and H. L. Tsai, J. Heat Transfer **129**, 1025 (2007).
[30] J. Hu and H. L. Tsai, J. Appl. Phys. **100**, 053304 (2006).
[31] J. Hu, H. Guo, and H. L. Tsai, Int. J. Heat Mass Transfer **51**, 2537 (2008).
[32] T. Zacharia, A. H. Eraslan, D. K. Aidun, and S. A. David, Metall. Trans. B **20**, 645 (1989).
[33] Z. Cao, Z. Yang, and X. L. Chen, Weld. J. **83**, 169s (2004).
[34] G. Speckhofer and H. P. Schmidt, IEEE Trans. Plasma Sci. **24**, 1239 (1996).
[35] S. M. Aithal, V. V. Subranmaniam, J. Pagan, and R. W. Richardson, J. Appl. Phys. **84**, 3506 (1998).
[36] J. F. Lancaster, *The Physics of Welding*, 2nd ed. (Pergamon, Oxford, 1986).
[37] S. V. Patanka, *Numerical Heat Transfer and Fluid Flow* (McGraw-Hill, New York, 1980).
[38] Y. S. Kim and T. W. Eagar, Weld. J. **72**, 269s (1993).
[39] Y. H. Kang and S. J. Na, Weld. J. **81**, 8s (2002).
[40] L. A. Jones, T. W. Eagar, and J. H. Lang, Weld. J. **77**, 135s (1998).